

A First Principles Investigation of Native Interstitial Diffusion in Cr_2O_3

Bharat Medasani^a, Maria L. Sushko^a, Kevin M. Rosso^a, Daniel K. Schreiber^b, Stephen M. Bruemmer^b

^aPhysical and Computational Sciences Directorate, Pacific Northwest National Laboratory, Richland, WA 99354, USA

^bEnergy and Environment Directorate, Pacific Northwest National Laboratory, Richland, WA 99354, USA

Abstract

First principles density functional theory (DFT) investigation of native interstitials and the associated self-diffusion mechanisms in $\alpha\text{-Cr}_2\text{O}_3$ reveals that interstitials are more mobile than vacancies of corresponding species. Cr interstitials occupy the unoccupied Cr sublattice sites that are octahedrally coordinated by 6 O atoms, and O interstitials form a dumbbell configuration orientated along the [221] direction (diagonal) of the corundum lattice. Calculations predict that neutral O interstitials are predominant in O-rich conditions and Cr interstitials in +2 and +1 charge states are the dominant interstitial defects in Cr-rich conditions. Similar to that of the vacancies, the charge transition levels of both O and Cr interstitials are located deep within the bandgap. Transport calculations reveal a rich variety of interstitial diffusion mechanisms that are species, charge, and orientation dependent. Cr interstitials diffuse preferably along the diagonal of corundum lattice in a two step process via an intermediate defect complex comprising a Cr interstitial and an adjacent Cr Frenkel defect in the neighboring Cr bilayer. This mechanism is similar to that of the vacancy mediated Cr diffusion along the c-axis with intermediate Cr vacancy and Cr Frenkel defect combination. In contrast, O interstitials diffuse via bond switching mechanism. O interstitials in -1 and -2 charge states have very high mobility compared to neutral O interstitials.

1. Introduction

The global cost of corrosion is estimated to be US \$2.5 trillion annually [1]. To prevent corrosion, many Ni and Fe-based alloys utilize Cr as an alloying element due to its ability to form Cr_2O_3 as a protective oxide coating [2, 3, 4, 5, 6]. These alloys are often used in extreme operating conditions such as in nuclear reactors, where the irradiating conditions can create defects within the protective oxide film, or in turbine blades with high operating temperatures. The effectiveness of these alloys under such extreme conditions has been the subject of many experimental studies [7, 8]. Understanding the mechanism and the limits of corrosion protection offered by Cr_2O_3 requires detailed atomistic models of defect formation and transport in this oxide. Towards this objective, many experimental studies of defects, oxidation mechanisms, and diffusion in Cr_2O_3 were carried out [9, 10, 11, 12, 13, 14, 15]. Some of these studies indicated that Cr interstitials could be the dominant defects in Cr_2O_3 under reducing conditions [14, 15]. Classical Monte Carlo simulations also predicted that Cr interstitials had lower barrier energies and, therefore, higher mobility than vacancies [16]. These studies suggest that interstitials could be controlling the effectiveness of Cr_2O_3 as a protective layer in pressurized water reactors (PWR), where reducing conditions prevail due to the use of hydrogenated water as a coolant.

Advances in experimental, theoretical and computational methods led to a renewed focus on defects and their diffusion mechanisms in Cr_2O_3 in recent years [17, 18, 19, 16, 15, 20, 21]. Within the last decade, first principles density functional theory (DFT) [22, 23, 24] has emerged as a reliable tool to model point defects in bandgap materials in part due to the development of *a posteriori* correction techniques [25]. However, DFT simulations of defects and their diffusion in Cr_2O_3 were focused exclusively on vacancies [17, 18, 19], while diffusion of interstitials defects has not been studied. To obtain a comprehensive atomistic picture of native defects and their diffusion in Cr_2O_3 , here, we investigated Cr and O interstitials in Cr_2O_3 in the charge states ranging between [0, 3] and [-2, 0], respectively, using density functional theory and identified their diffusion mechanisms and pathways.

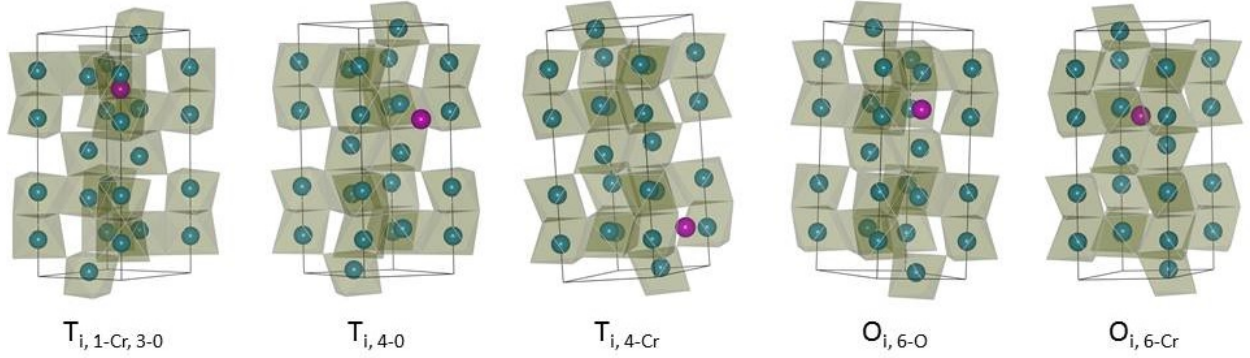


Figure 1: Potential interstitial sites (magenta spheres) for Cr_2O_3 obtained from PyCDT [26]. T_i and O_i designations represent tetrahedral and octahedral sites respectively. The subscript identifies the type and number of coordinating elements. Teal spheres represent Cr atoms and the O atoms are at the vertices of the octahedra surrounding the Cr atoms.

2. Methods

2.1. Interstitial Site Selection

Table 1: Correspondence between the Kroger-Vink (K-V) representation and the representation used in this work for charged interstitials.

Defect	Charge	K-V Notation	Notation in this study
Cr interstitial	0	Cr_i^X	Cr_i^0
	1	Cr_i^\bullet	Cr_i^1
	2	$\text{Cr}_i^{\bullet\bullet}$	Cr_i^2
	3	$\text{Cr}_i^{\bullet\bullet\bullet}$	Cr_i^3
O interstitial	0	V_O^X	V_O^0
	-1	O_i'	O_i^{-1}
	-2	O_i''	O_i^{-2}

evaluating the coordination pattern at each grid point. Grid points that exhibit the coordination patterns resembling basic structural motifs (e.g., tetrahedral and octahedral environments) with high symmetry are identified by this algorithm as potential interstitial sites.

2.2. Density Functional Calculations

Interstitials were modeled with periodic supercell formalism. For charged interstitials, neutralizing background charge was automatically added by the DFT software, making the supercells neutral. Geometry relaxation, barrier energy, and phonon calculations for this study were performed within the DFT framework implemented in the Vienna *ab initio* simulation package (VASP) [29, 30, 31]. We included Hubbard on-site Coulombic correction (U) using GGA+U method[32, 33]. The basis sets of Cr and O consist of 12 and 6 valence electrons in the configurations of $[\text{He}]2s^22p^4$ and $[\text{Ne}]3s^2]3p^64s^23d^4$ respectively. Further details of GGA+U simulations are given in Supplementary Information (SI). The DFT settings used in this study were unchanged from those used in our previous work on vacancies in Cr_2O_3 [18], and the bulk properties of Cr_2O_3 obtained with these settings can be found in our previous publication. [18]

This work is a continuation from our previous study of vacancies and vacancy mediated self-diffusion in Cr_2O_3 [18]. Therefore, the methods and associated parameters used in this study are the same as those in our study on the vacancies in Cr_2O_3 . The notation used in this work for interstitials with different charge states and the corresponding Kroger-Vink notation are provided in Table 1. We used PyCDT [26] and pymatgen [27] to identify potential interstitial sites in Cr_2O_3 . The interstitial finding procedure [28] implemented in pymatgen systematically performs a grid based search for potential interstitial sites by

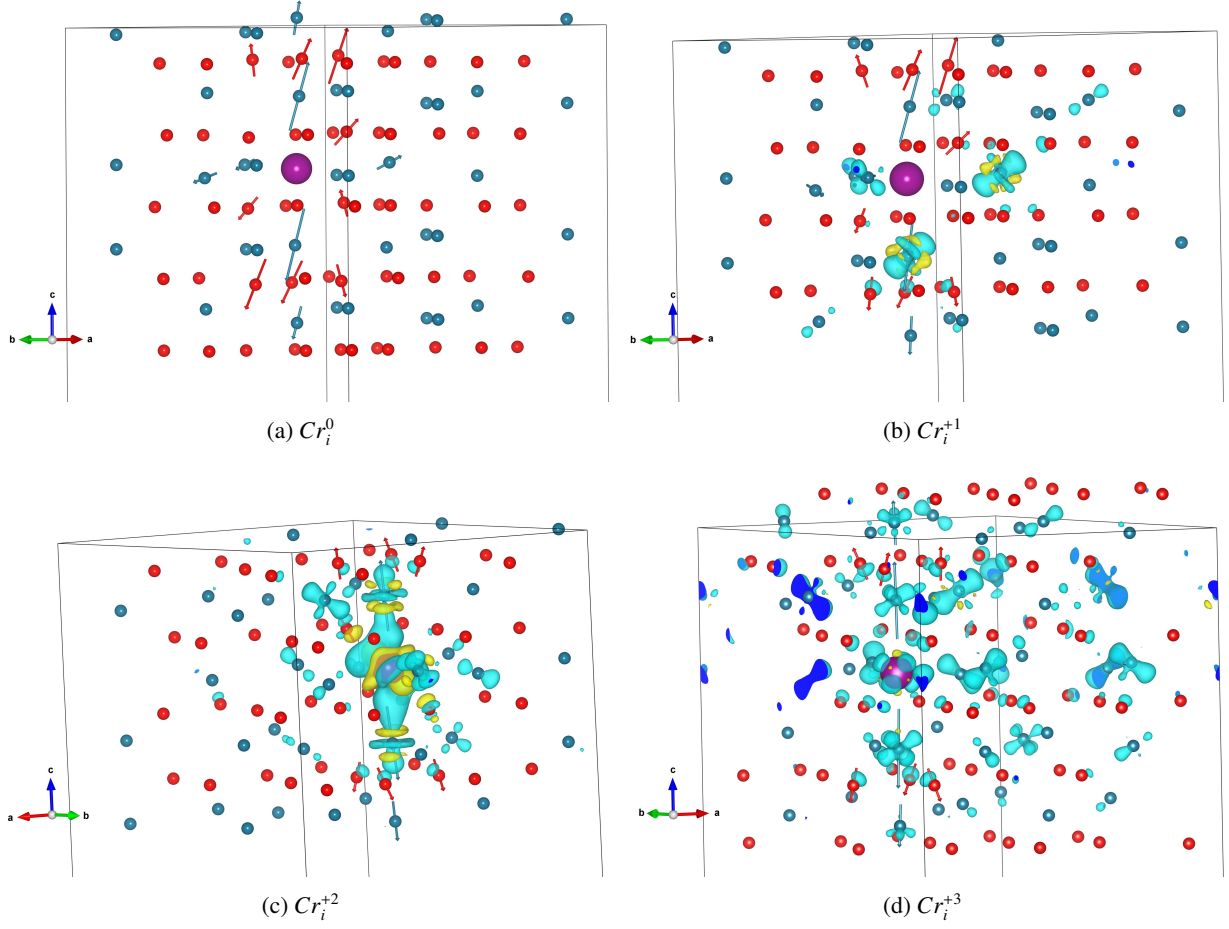


Figure 2: Relaxed geometry surrounding the Cr interstitial (denoted with magenta sphere) for different charge states. For non-zero charge states, the density of the hole charge is also plotted. The teal and red arrows indicate the displacement of Cr and O ions respectively. Yellow and blue isosurfaces indicate the excess or deficit electronic charge at 5 millielectrons/ \AA^3 .

We used the thermodynamic formalism proposed by Zhang and Northrup [34] to evaluate the formation energies of the interstitials. The formation energy of an interstitial of species X with charge q , $E_f(X_i^q)$, was calculated as

$$E_f(X_i^q) = E_{tot}(X_i^q) - E_{tot}[bulk] - \mu_X + qE_F + E_{corr}, \quad (1)$$

where $E_{tot}(X_i^q)$ is the total energy of the defect supercell, $E_{tot}[bulk]$ is the total energy of the bulk supercell, μ_X is the chemical potential contribution resulting from the removal of the atom/ion of species X , E_F is the Fermi level and E_{corr} is the correction term, which encompasses the correction to finite-size electrostatic interactions and bandgap underestimation in DFT [18]. The barrier energies were computed using CI-NEB method [35].

The stability of predicted interstitial sites and transition states was evaluated using phonon density of states (PDOS) calculations. The PDOS of stable interstitial sites should exhibit no imaginary frequencies, while the transition states, being saddle points, should have one imaginary frequency in their PDOS. Additional details about the phonon calculations are provided in the SI.

In addition to PyCDT and pymatgen, we utilized phonopy [36], and VESTA [37] for generating inputs to DFT calculations, post-processing, and plotting the DFT calculations results.

3. Results and Discussion

3.1. Potential Interstitial Sites

The order-parameter based interstitial finding algorithm introduced by Zimmerman et al. [28] identified five potential interstitial sites and their positions are shown in Figure 1. Among the potential interstitial sites, three are tetrahedral sites and the remaining two are octahedral sites, which are defined by their coordination numbers as well as the coordinating elements. $O_{i,m-Cr,n-O}$ represents an octahedral interstitial site surrounded by m Cr sites and n O sites. Similarly $T_{i,m'-Cr,n'-O}$ represents a tetrahedral interstitial site with m' Cr sites and n' O sites as neighbors. Of these sites, the $T_{i,3-Cr,1-O}$ site was found to be too close to the regular corundum lattice sites and ignored. The remaining four sites were populated either by Cr or O and the structure of the resultant defect supercells were optimized. The Cr and O interstitial defects were initially assigned with charge states in the range of $[0,6]$ and $[-2, 0]$ respectively.

The resulting uncorrected interstitial formation energies are shown in Figure S1 in SI. The large differences in the calculated formation energies for the different interstitial positions in the lattice indicate that $O_{i,6-O}$ site is the most favorable interstitial site for both O and Cr interstitials (denoted as $O_{i,oct,06}$ and $Cr_{i,oct,06}$ respectively). Hence for further analysis, we considered only the 6-O coordinated octahedral interstitial site. Further on, we use standard notation of Cr_i and O_i for Cr and O interstitials at the 6-O coordinated octahedral site instead of $Cr_{i,oct,06}$ and $O_{i,oct,06}$, respectively. The uncorrected formation energies Cr_i for charge states of 4, 5 and 6 are very high when compared to those of the charge states in the range $[0, 3]$, and hence the charge states of 4–6 for Cr_i are ignored in this study.

3.2. Interstitials

The relaxed interstitial structures shown in Figure 2 indicate that Cr interstitials occupy the unoccupied octahedral sites in the Cr bilayer coordinated by the O sublattice. In contrast, the O interstitials shown in Figure 3 relax to a dumbbell configuration with each of the O ion in the dumbbell lobes residing at the unoccupied octahedral sites.

The effect of interstitial charge on the displacement of the lattice ions around the interstitial is shown by the ion displacement vectors in Figures 2 and 3 and the magnitudes of ionic displacements are summarized in Tables S1 and S2 in SI for Cr and O interstitials, respectively. The relaxation of the ions

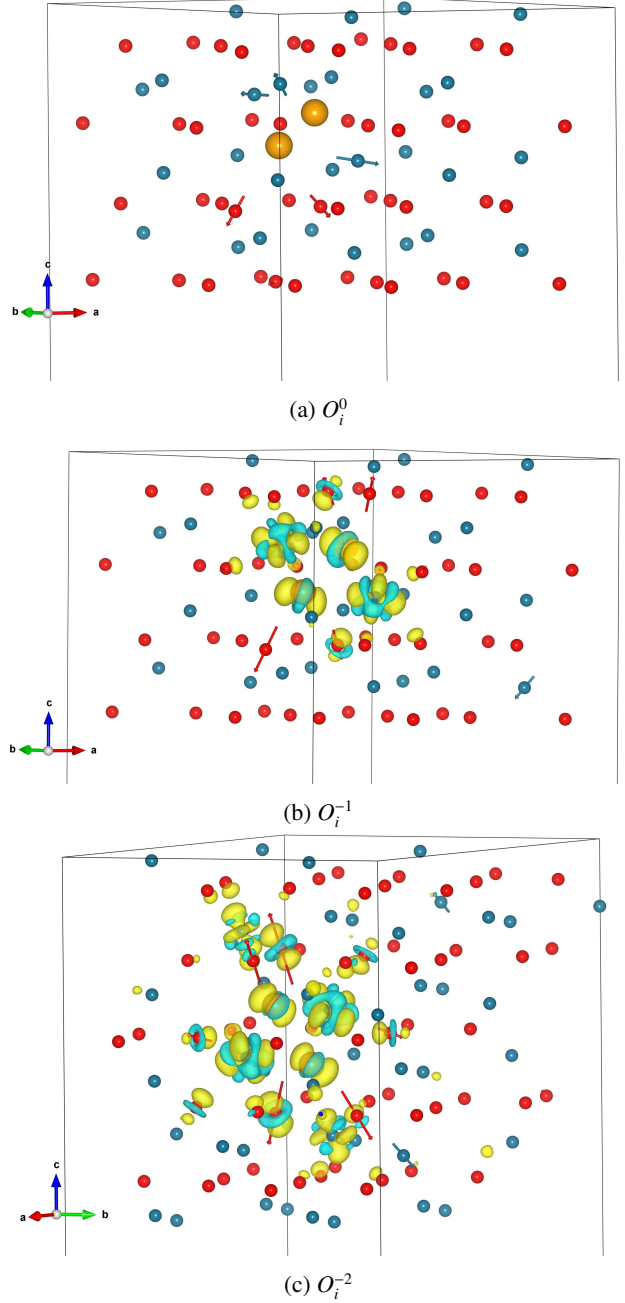


Figure 3: Relaxed geometry surrounding the O dumbbell interstitial (denoted with orange spheres) for different vacancy charge states. For charged O_i , the distribution of excess electrons is also plotted. The teal and red spheres and the corresponding arrows indicate the Cr and O ions and their displacements respectively. Orange spheres indicate the dumbbell interstitial. Yellow and blue isosurfaces indicate the excess or deficit electronic charge at 5 millielectrons/ \AA^3 .

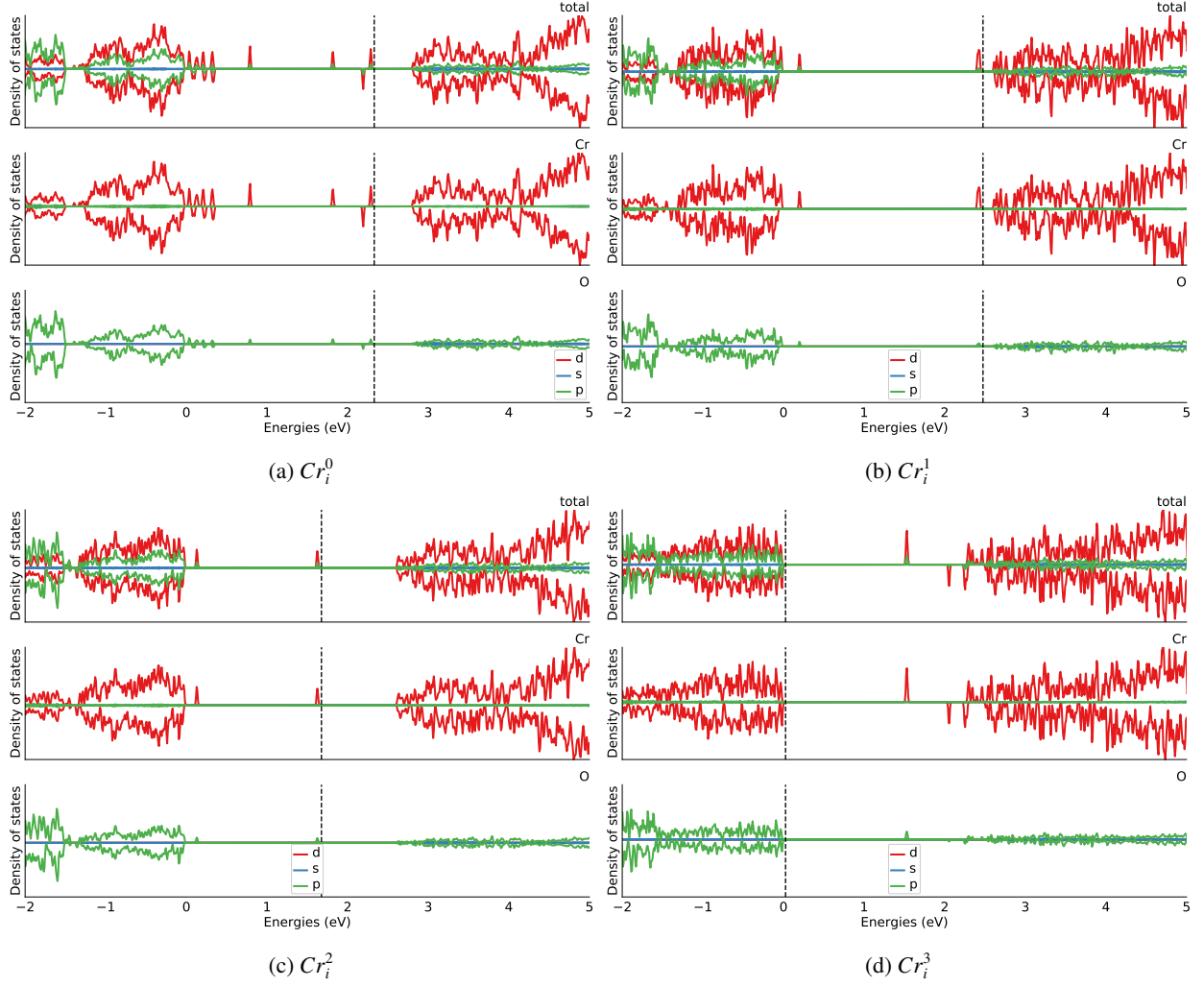


Figure 4: Element projected orbital density of states averaged over all sites for Cr interstitials in different charge states. Dashed vertical line marks the position of the Fermi level.

surrounding the interstitials was found to be anisotropic. The nearest Cr ions to a Cr interstitial shift away from the interstitial with the maximum displacement at 0.3 \AA . The amount of displacement was found to be dependent on the interstitial charge and the distance of the ions from the interstitial. In particular, the nearest O ions have an outward displacement of up to 0.22 \AA except in the case of Cr_i^3 , where the nearest O ions move towards the Cr interstitial by $0.12 - 0.15 \text{ \AA}$. For neutral O interstitials, only two Cr ions that are at 1.9 \AA distance move away from the interstitial. For charged O interstitials, O ions at 2.7 and 2.9 \AA distance are displaced by 0.36 \AA and 0.23 \AA respectively for -2 charge, and undergo even less shifting for $q = -1$. The relatively small magnitude of displacements and the small number of ions with any noticeable displacement indicate that interstitials do not introduce any significant local distortion in the lattice of Cr_2O_3 .

To evaluate the localization of holes in charged Cr_i and electrons in charged O_i , the difference between charge distribution in a charged interstitial and the charge distribution of the corresponding neutral interstitial with identical structure is plotted in Figures 2 and 3. In some of the previous studies of defects in oxides with excess holes, a non-zero Hubbard correction in the range of $4.0 - 5.5 \text{ eV}$ was applied for O-2p orbitals to properly account for the hole charge distribution[38, 39, 40]. However, in undoped Cr_2O_3 , applying $U_{O_{2p}} = 5$, did not produce any noticeable difference in the hole charge distribution (see Figure S2 in SI). For Cr_i^1 , the hole charge shown in Figure 2b is mainly

localized on two lattice Cr ions closest to the interstitials located at a distance of 2.45 Å along the c-axis and 2.99 Å in the basal plane from the interstitial. The major portion of the remaining hole charge is localized on two Cr ions in the basal plane at a distance of 2.94 Å from the interstitial. In the case of Cr_i^2 , the majority of the 2-hole charge is localized on the Cr interstitial itself. Some of the hole charge is distributed on the two nearest Cr ions along the c-axis at 2.4 Å, two Cr ions in the basal plane at 2.94 Å and two Cr ions at 3.8 Å along the [221] direction. For Cr_i^3 , the 3-hole charge

The charge distribution plots of excess holes indicate that the holes are neither completely localized on individual ions nor completely delocalized. This result is consistent with the predictions of Lany [41] and Kehoe et al [39]. According to Lany, the non-bonding Cr-3d t_{2g} orbitals at the top of the valence band are responsible for the delocalized nature of the holes. The holes in Cr_2O_3 are predicted to be band conducting with heavy effective mass [41].

The excess electron density of O_i^{-1} is localized mainly on the O ions forming the lobes of a dumbbell interstitial and the two nearest Cr ions. For O_i^{-2} , the excess 2-electron charge is also distributed over the adjacent Cr and the O ions in the basal planes that are at 2.4 – 2.5 Å distance from either of the interstitial O ions.

The electronic density of states (DOS) plots of the optimized Cr and O interstitial structures are presented in Figures 4 and 5, respectively. The computed bandgap in these figures is 2.8 eV [18]. The plots reveal that the energy states corresponding to both Cr and O interstitials are located in the bandgap, and are of hybrid O- p and Cr- d character, which is similar to the nature of the vacancy states [18]. The defect levels of the neutral Cr interstitial, which are located in both the lower and upper parts of the bandgap, are occupied with electrons and the Fermi level is closer to the conduction band. For positively charged Cr interstitials, the unoccupied defect levels are shifted up on the energy scale. The upward shift of the empty interstitial levels increases with the charge of Cr interstitial. This effect can be attributed to the reduction in their screening due to the loss of electrons. For Cr_i^3 , the majority of the defect levels are empty and are shifted closer of the conduction band.

The DOS plots of O_i indicate that occupied O_i^0 levels are located at the bottom of the bandgap region near the valence band maximum (VBM) (Figure 5). The unoccupied O_i^0 levels are in resonance with the conduction band. When the O_i interstitial charge is increased negatively, the interstitial gains electrons and the newly occupied defect levels shift down towards the center of the bandgap. For O_i^{-2} , the occupied defect levels reside in the lower half of the bandgap. Interestingly, the highest occupied level of O_i^{-1} is higher than that of the O_i^{-2} and is characterized by spin splitting of the defect levels. Such relative position of defect levels can be attributed to the relatively lower screening experienced by highest occupied defect level in O_i^{-1} compared to that of O_i^{-2} .

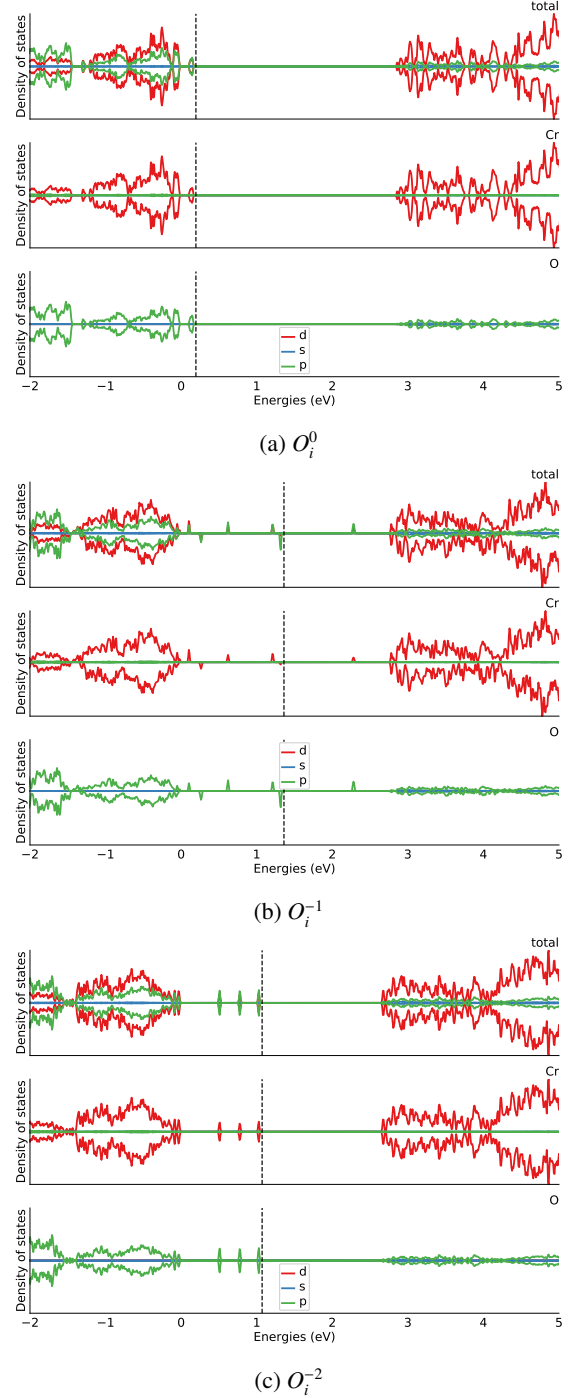


Figure 5: Element projected orbital density of states averaged over all sites for O interstitials. Dashed vertical line marks the position of the Fermi level.

The interstitial formation energies were corrected for electrostatic interactions between periodic images of charged simulation cells and for the under-predicted DFT bandgap. Electrostatic corrections were obtained using anisotropic FNV (Freysoldt, Neugebauer, and Vande Walle) method [42, 43] (see Table S3 in SI for details). The transition levels of Cr and O interstitials with respect to the VBM were corrected for the DFT bandgap error using the scheme proposed by Janotti and Vande Walle[44]. The resulting corrections to the transition levels and the associated corrections to the interstitial formation energies are summarized in SI Tables S4 and S5, respectively. The resultant formation energies were plotted with respect to the position of the Fermi level in Figure 6 for both O-rich and Cr-rich conditions. These conditions were defined by the upper and lower limits of Cr and O chemical potentials determined in our previous study [18]. Here, we focused on the 0 K DFT computed phase stability, and the investigation of the effect of p_{O_2} and temperature on interstitial formation energies is deferred to a future study.

The formation energies reveal that for Cr-rich and p-type conditions, as the Fermi level is in the lower half of the bandgap, Cr interstitials are energetically more favorable compared to O interstitials. Under n-doped conditions, corresponding to the Fermi level being in the upper half of bandgap, O interstitials become the dominant interstitial defects even in Cr rich conditions (Figure 6). However, under n-doped, Cr-rich conditions, both V_{Cr} and V_O have lower formation energies than interstitials. For O rich conditions, O interstitials are energetically more favorable over Cr interstitials under all doping conditions. The transition levels of both Cr and O interstitials, which are denoted as stars in the Figure 6 (see also the last column of SI Table S4), are deep in the bandgap. While the $Cr_i +3/+2$ transition level is very deep and 1.64 eV above VBM, the other transition levels are relatively shallow and are less than 0.6 eV below the conduction band minimum (CBM). The predicted transition levels for O interstitials (last column of SI Table S4) indicate that either of neutral or -2 charge states has lower formation energy when compared to -1 charge state at any Fermi level in the bandgap. The phonon DOS plot in SI Figure S4 (a) shows that O_i^{-1} is a stable defect with no soft modes. This suggests that the concentration of O_i^{-1} would be relatively insignificant under any physical condition.

Our grand canonical calculations of defect chemistry at finite temperatures (Figure S3 and S4 in SI) indicate that undoped Cr_2O_3 is a stable semiconductor with the Fermi level located in the center region of the band gap. Our calculations predict that at high temperatures (> 800 K), intrinsic Cr_2O_3 is weakly n -type and at low (300 – 400 K) and intermediate (400 – 800 K) temperatures, intrinsic Cr_2O_3 is slightly p -type. When Cr_2O_3 acts as a protecting layer on a metal substrate, the metal-oxide boundary has effectively very low p_{O_2} . At low p_{O_2} , the formation energies of V_O and V_{Cr} at $E_F = 1.7$ eV, are equal to 2.6 eV and 4.0 eV respectively [18], and are lower than those of Cr_i and O_i , which are equal to 5.3 and 5.6 eV, respectively. This indicates that at low p_{O_2} , V_O could be the dominant defect in undoped Cr_2O_3 followed by V_{Cr} . This contradicts the conclusions from some of the experimental studies on

Table 2: Interstitial formation energies (in eV) of Cr_2O_3 with Fermi level (E_F) at 0.1 eV above VBM, 0.1 eV below CBM, and in the middle of the bandgap.

Defect ($E_F =$)	q	Interstitial Formation Energy					
		VBM+0.1 eV		CBM-0.1 eV		VBM+ $E_g/2$	
		Cr rich	O rich	Cr rich	O rich	Cr rich	O rich
O_i	0	5.57	2.18	5.57	2.18	5.57	2.18
	-1	8.69	5.29	5.49	2.09	7.09	3.69
	-2	10.98	7.58	4.58	1.18	7.78	4.38
Cr_i	0	7.51	10.13	7.51	10.13	7.51	10.13
	1	4.60	7.21	7.80	10.42	6.20	8.82
	2	2.09	4.71	8.49	11.11	5.29	7.91
	3	0.55	3.17	10.15	12.77	5.35	7.97

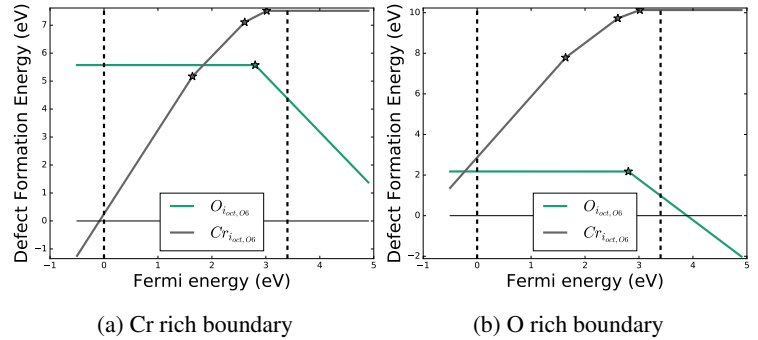


Figure 6: Formation energies of Cr and O interstitials after applying electrostatic and bandgap related corrections. Black solid line corresponds to $E_f(Cr_i)$ and green dashed line refers to $E_f(O_i)$. The dashed vertical lines denote the edges of bandgap region with 0-level representing valence band maximum (VBM).

self-diffusion in Cr_2O_3 [14, 15], where V_O and Cr_i were suggested as the dominant defects in Cr_2O_3 at very low p_{O_2} . It is noteworthy, that Cr_2O_3 passivation films on Ni alloy substrate could be p-type doped due to trace amounts of Ni substitution [40]. For Ni doping, Fermi level in Cr_2O_3 stabilizes at 0.4 eV above VBM [40]. Under such conditions, Cr_i defects have lower formation energy compared to V_{Cr} and both Cr_i and V_O have formation energies approximately equal to 1.5 eV, making Cr_i and V_O the dominant defects. Similarly, bulk Cr_2O_3 samples can be strongly p-type doped with E_F close to VBM, when divalent ions such as Mg are present as impurities [40]. Under such conditions, our calculations suggest that Cr_i could be the dominant defect in bulk Cr_2O_3 in place of V_{Cr} . Based on these results, the Cr_2O_3 samples used Ref.14 and 15 could be inadvertently p-type doped due to trace impurities. Furthermore, the presence of either an additional spinel layer or hydrogenated water opposite to the metal-oxide side could result in reducing conditions for the entire Cr_2O_3 layer in the PWR environments. In such conditions, the dominant defects could be either Cr interstitials or Cr vacancies depending on the Fermi level.

With vacancies included, under heavily oxidizing conditions, O_i and V_{Cr} are the dominant defects. When the Fermi level is above 2.2 eV, Cr_2O_3 is unstable against V_{Cr} [18] indicating that compensating Cr vacancies will form if Cr_2O_3 is heavily doped with electron donating species. Under p-doped conditions, V_{Cr} and O_i both have formation energies of 2.0 eV, indicating that both defects have near equal concentrations. For both defects, neutral charge state is the dominant charge state under p-doped conditions.

3.3. Interstitial Diffusion

3.3.1. Cr_i diffusion

We have studied the diffusion of Cr and O interstitials in charge states ranging from [0, 3] and [-2, 0], respectively. The preferential diffusion pathways for both Cr and O interstitials are identified to be either in the basal plane or along the diagonal of the standard corundum lattice.

Figure 7 illustrates the Cr diffusion pathways studied. In this figure the magenta spheres represent the initial and final Cr interstitial sites and the blue spheres represent Cr ions affected by interstitial diffusion process. Interstitial diffusion typically involves two mechanisms: direct and interstitialcy diffusion. In the direct mechanism, shown as dotted lines in Figure 7, a Cr ion hops from one interstitial site to an adjacent interstitial site squeezing through the ions in the regular lattice. In the interstitialcy mode, a Cr interstitial knocks off a Cr ion in the regular Cr sublattice (represented by one of the two blue spheres) and occupies that sublattice site. The displaced Cr ion goes to a neighboring unoccupied interstitial site. We investigated both the pathways using CI-NEB method. However, either convergence could not be obtained in CI-NEB calculations, or the resulting barrier energies were very high (greater than 5 eV). This led us to investigate an alternative interstitial diffusion mechanism. In this mechanism, diffusion is accomplished in two stages and involves an intermediary metastable configuration. In the first stage, either one of the Cr ions along the diffusion path (represented by blue spheres) jumps to the final interstitial position. This jump creates a defect complex comprising a Cr Frenkel pair and a Cr interstitial. This defect complex is quite similar to the intermediate triple defect (Cr Frenkel pair + Cr vacancy) involved in vacancy mediated Cr diffusion along c-axis [18]. During the second step, Cr in the initial interstitial site jumps to the vacated Cr lattice site, thereby completing the diffusion process. This mechanism also resulted in lower barrier energies (for example, by ~ 2 eV for Cr_i^3 along [221]) compared to direct and interstitialcy mechanisms in the few cases where CI-NEB calculations of direct and interstitialcy mechanisms

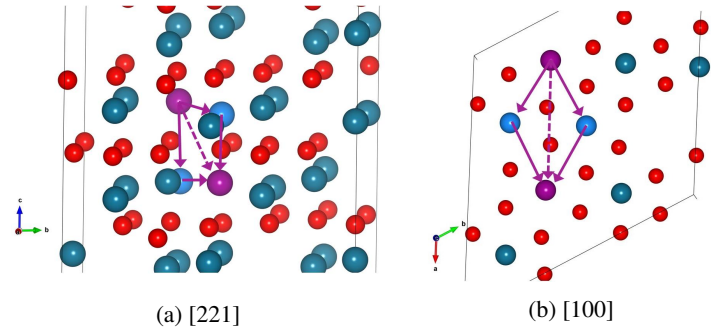


Figure 7: Migration pathways considered for Cr interstitial diffusion along (a) [221] (diagonal to corundum lattice) and (b) [100] directions. Magenta spheres represent the initial and final Cr interstitial positions. The dotted line represent the direct hopping pathway, which could not be evaluated. The solid lines represent the paths, where the blue spheres hop to the final magenta sphere and create an intermediary defect complex comprising of interstitial and Frenkel defect. Teal and red spheres denote the regular Cr and O ions. Plot (a) is oriented along side view and plot (b) is oriented along top view for clarity.

Table 3: Migration barriers for Cr interstitial mediated diffusion. q denotes interstitial charge state.

Diffusion Path ($q =$)	Length (Å)				Attempt Frequency (THz)				Migration barrier (eV)			
	0	1	2	3	0	1	2	3	0	1	2	3
[100]	4.96	4.97	4.99	4.99	—	—	—	—	4.04	5.53	8.21	5.2
[221]	3.81	3.81	3.74	3.74	5.39	8.71	10.23	76.89	2.26	1.86	2.62	3.69

converged implying that it is the true Cr interstitial diffusion mechanism in Cr_2O_3 . It may also represent one of the modes of cations interstitial diffusion in other corundum sesquioxides. For both the interstitialcy and the proposed mechanisms, the atoms involved in the diffusion and their initial and final positions are the same. The difference is that in the interstitialcy mechanism both atoms move concurrently, while in the mechanism proposed in this work, they move consecutively.

Figure 7a shows the diffusion pathway for Cr diffusion along the [221] direction. Diffusion involves either the Cr ion adjacent to the interstitial in the same Cr bilayer or the Cr ion in the next bilayer hopping to the final interstitial site. Depending on the Cr ion involved, elementary diffusion takes place either along the c -axis or along the basal plane, respectively. The subsequent jump by the second ion is then along the basal plane or the c -axis, respectively. Figure 7b shows the diffusion pathway for Cr diffusion along basal plane (shown for [100] direction but also applies to [010] direction). In the first stage, one of the six neighboring Cr ions of the occupied interstitial jumps to one of the two available unoccupied interstitial sites. A total of 4 interstitial sites (two along [100] and two along [010]) are available for all the neighboring Cr ions.

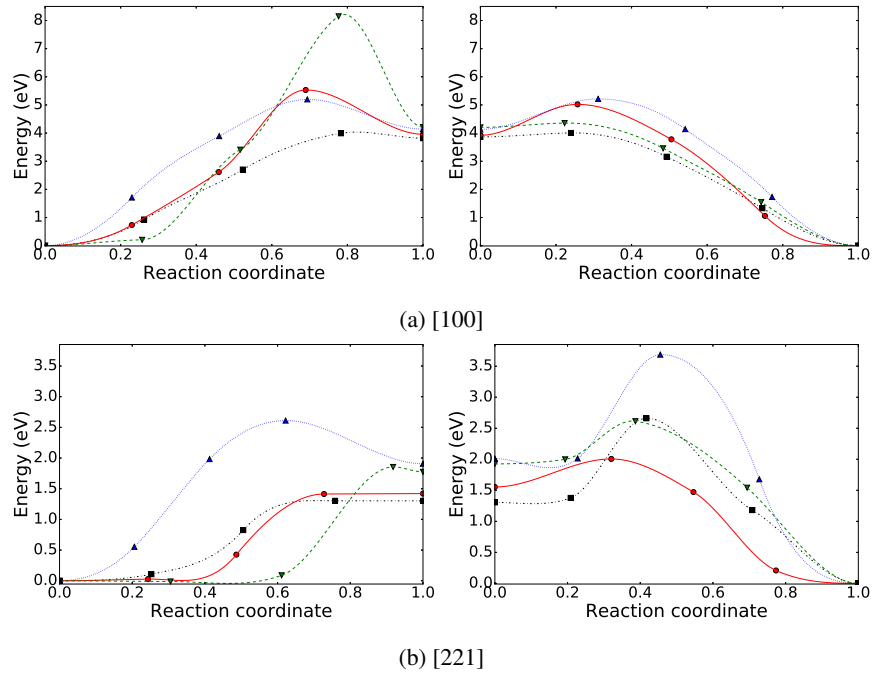


Figure 8: Migration barriers of Cr interstitial diffusion along (a) [100] and (b) [221] pathways. Black, red, green, and blue lines represent Cr_i^0 , Cr_i^1 , Cr_i^2 , and Cr_i^3 , respectively.

NEB barrier energy plots for Cr diffusion along [100] and [221] directions are shown in Figure 8. The left hand side and right hand side plots correspond to the first and second stages of the Cr interstitial diffusion, respectively. The plots reveal that Cr interstitials preferentially diffuse along the diagonal of the corundum lattice, in contrast to Cr vacancies that diffuse along the basal plane [18].

The calculated barrier energies for Cr diffusion along [100] reveal that Cr_i^0 diffusion incurs the lowest barrier of 4.04 eV (Figure 8a and Table 3) followed by that for Cr_i^3 , Cr_i^1 , and Cr_i^2 . Out of the interstitials studied, Cr_i^1 , Cr_i^2 have higher barrier energies for the first stage of [100] diffusion compared to that for the second stage. In contrast, Cr_i^0 and Cr_i^3 exhibit nearly equal barrier energies for both stages of diffusion. Assuming the metastable defect complex as reference point, the nearly equal barrier energies imply that either of the Cr interstitials in the initial and final positions can jump to the vacant Cr site with equal probability. However, jumping back of the Cr interstitial in the final position does not result in net diffusion. Hence a prefactor of 0.5 needs to be added to the diffusion coefficient for Cr_i^0 and Cr_i^3 .

Table 4: Migration barriers for O interstitial mediated diffusion. q denotes vacancy charge state.

Diffusion Path ($q =$)	Length (Å)			Attempt Frequency (THz)			Migration barrier (eV)		
	0	-1	-2	0	-1	-2	0	-1	-2
[100]	2.12	2.53	2.09	54.98	2.73	6.35	1.52	2.12	0.30
[221] short	2.34	2.25	2.23	27.15	2.13	6.77	1.27	0.21	0.29
[221] long	3.45	3.2	3.12	–	6.34	48.12	–	1.63	0.58

Simulations of Cr interstitial diffusion along [221] suggest that Cr_i^1 has the lowest diffusion barrier of 1.86 eV (Figure 8b and Table 3) followed by Cr_i^2 , Cr_i^0 , and Cr_i^3 . In contrast to Cr diffusion along [100] direction, [221] diffusion is characterized by relatively higher barrier energies for the second stage of the diffusion when compared to the first stage. However, we believe this difference is solely due to our choice of the ion (from the two ions available) involved in the first stage of the diffusion.

Compared to Cr vacancies, which have the lowest diffusion barrier energies of 2.01 eV (V_{Cr}^{-3} along basal plane) [18], Cr interstitials have even lower barrier energies of 1.86 eV (Cr_i^1 along [221]). The 0.15 eV lower barrier implies that Cr interstitials are more mobile than Cr vacancies by two orders of magnitude at room temperature. At very high temperatures (around 1200 K), the difference in the energy barriers becomes comparable to the thermal energy and both Cr interstitials and vacancies have effectively equal mobilities.

It would be of interest to the community to identify physical factors that could be used either as descriptors to predict the barrier energies or to explain the variations in the barrier energies for different charge states. Lei and Wang [45], in their study of barrier energies of vacancies in Al_2O_3 , identified a correlation between barrier energies and the change in defect levels of the vacancies between transition and ground states. Following that approach, we compared the barrier energies with the differences in the defect levels (Figure S6 of SI for transition state DOS) and also the differences in the electrostatic potentials (Table S6 of SI) experienced by the diffusing ion at the transition states of the [221] pathway and the interstitial ground states for Cr_i diffusion. Unlike the case of Al_2O_3 , in Cr_2O_3 no such correlation could be found between the barrier energies of Cr_i and either of the two physical factors examined. Similarly, no such correlation was found for O_i also, which are discussed in the following section (see Figures S7-S9 and Table S6 in SI). The barrier energies for both Cr_i and O_i are a result of complex interplay of variations in local geometrical distortion, electrostatic potentials, and electronic correlation effects.

3.3.2. O_i diffusion

An O interstitial forms a dumbbell configuration oriented along [221] around a regular O site. O ion diffusion is accomplished by bond switching, where one of the interstitial O ions jumps to one of the nearest O sites and forms a dumbbell configuration with the lattice O ion. The remaining O ion at the initial interstitial location returns to its regular lattice position.

O diffusion pathways considered in this study are shown in Figure 9. The red spheres in Figure 9a represent the O ions in the adjacent to the defect plane O layer and the labeled ions are the nearest to the upper O interstitial ion (dark orange sphere). The ions labeled with A' , A'' , and A''' represent three closest ions equidistant to the center of the dumbbell configuration in a perfect crystal. Of these A' is the closest site, followed by A'' and A''' . The sphere labeled as B represents the next closest O ion at around 3.1 – 3.5 Å from the dumbbell center, depending on the interstitial charge state. We computed the barrier en-

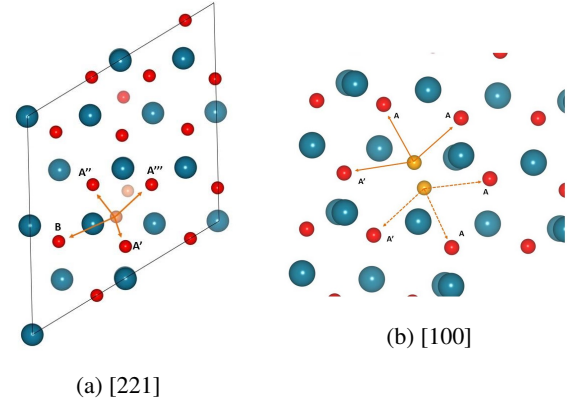


Figure 9: Migration pathways identified for O interstitial diffusion (via bond order switching) along (a) [221] (diagonal to corundum lattice) and (b) [100] directions. Orange spheres represent the O interstitial in dumbbell configuration. The view is from top (along c -axis) for both the plots. Teal spheres denote the Cr ions. For plot (a), dark red spheres represent O ions that are in the upper adjacent O-layer neighboring the O-layer consisting the O interstitial ions. For reference, one O-ion in the same layer of the interstitial O ions is shown in lighter red. In plot (b), the red spheres represent the O ions in the O-layer consisting of the O interstitial.

ergies associated with O_i diffusion to A' and B sites, denoted as [221]-short and [221]-long, respectively (Table. 4). In Figure 9b, the red spheres represent O ions in the same layer as the interstitial ions. Out of six nearest ions the ions represented by A are equidistant from the O interstitial and those denoted by A' are slightly farther away. The barrier energies were computed for O diffusion from interstitial site to A site.

O diffusion calculations show that O migration energies are highly dependent on the interstitial charge and the diffusion pathway (Figure 10). O_i^{-2} has the lowest barrier energies ranging from 0.29 to 0.58 eV. Further O_i^{-2} diffusion pathway encompasses one metastable state along [221]-short and [100] pathways and two metastable states in the [221]-long pathway. The metastable state corresponds to the diffusing O interstitial ion breaking bond with the other O-ion in the dumbbell and occupying the 6-O coordinated octahedral site. The identical phonon DOS plots of the transition states (Fig. S1 in SI) and the nearly equal barrier energies for [221]-short and [100] pathways indicate that both pathways have a common transition state for -2 charge state. O_i^{-1} has a significantly lower barrier energy of 0.21 eV along the [221]-short pathway when compared to the 1.63 eV and 2.12 eV energies along [221]-long and [100] pathways respectively. Neutral O_i on the other hand exhibits comparatively higher barrier energies around 1.5 eV for [221]-short and [100] pathways. We could not obtain convergence for O_i^0 diffusion along [221]-long path.

When compared to the O vacancies, O interstitials exhibit significantly lower barrier energies for diffusion. The lowest barrier energies of O vacancies are of the order of 1.2 – 1.5 eV for V_O^2 [18], whereas O_i^{-1} and O_i^{-2} have the lowest barrier energies of the order of 0.2 and 0.3 eV respectively. For the undoped Cr_2O_3 , however, consideration has to be given to neutral vacancies and neutral oxygen interstitials, because of their higher concentration at $E_F = E_g/2$. The neutral O interstitials are also significantly more mobile than neutral O vacancies with a 0.8 eV difference in the lowest barrier energies. It is noteworthy that under irradiation conditions, characterized by considerable and nearly equal in concentrations of interstitials and vacancies due to the formation of Frenkel defects, our results for barrier energies indicate that O interstitials could be responsible for oxygen transport in Cr_2O_3 .

4. Summary

To develop a comprehensive model of defect-mediated diffusion processes in Cr_2O_3 , we computed the electronic, thermodynamic, and diffusion properties of interstitials in Cr_2O_3 . This work is an extension to our previous study of vacancies in Cr_2O_3 . The formation energies of Cr and O interstitials in various charge states were evaluated for Cr-rich and O-rich conditions using the thermodynamic formalism proposed by Zhang and Northrup [34]. Our results indicate that Cr and O interstitials are deep defects, and contrary to vacancies, they do not generate any considerable local structural distortions.

O interstitials form dumbbell configurations and O diffusion is accomplished via bond switching mechanism. The computed migration barrier energies reveal that similar to vacancies, O interstitials are more mobile than Cr

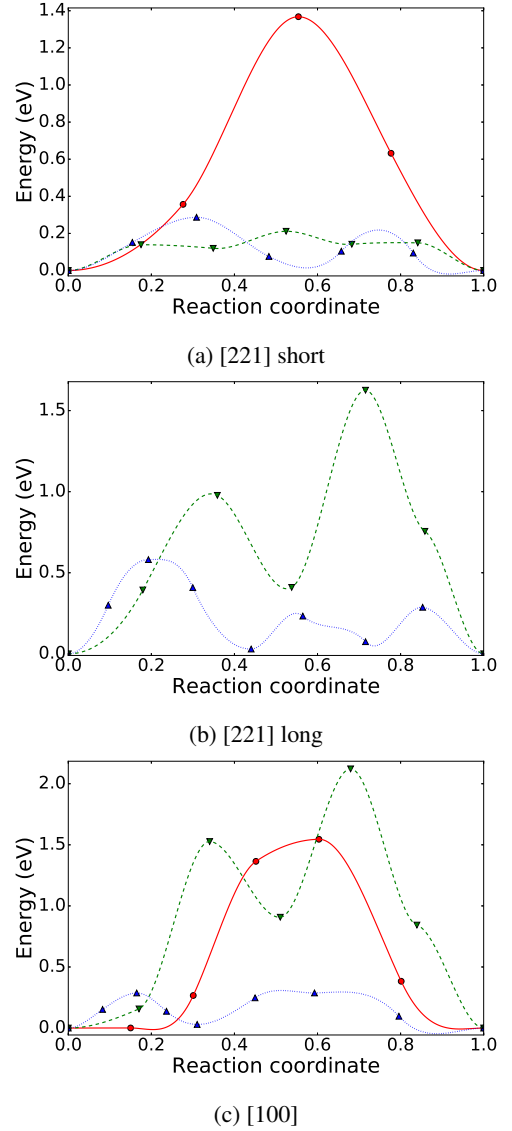


Figure 10: Migration barriers for O diffusion along (a) [221] short, (b) [221] long, and (c) [100] pathways. Red, green, and blue lines represent O_i^0 , O_i^{-1} , and O_i^{-2} respectively.

interstitials. Among different charge states of O interstitials, O_i^{-2} has the highest mobility for nearly all pathways. Overall, O interstitials are more mobile, i.e. incur lower barrier energies, than O vacancies.

Cr interstitials occupy the empty octahedral sites in the Cr sub-lattice and our calculations indicate that the preferred path for Cr interstitial diffusion is along [221] direction. The diffusion is accomplished via an intermediate metastable interstitial triple-defect configuration comprising a Cr interstitial and a Cr Frenkel defect in the adjacent Cr bilayer. Cr diffusion from one interstitial site to another site comprises two stages, with both basal and c-axis oriented diffusion happening in individual stages. The mobility of Cr interstitials is slightly higher but comparable to that of Cr vacancies.

The diffusion mechanisms of self-interstitials in Cr_2O_3 revealed in the present study can be used to understand the efficacy of Cr_2O_3 as a passivation layer and the corrosion mechanisms in Cr alloys under various physical conditions including irradiated conditions.

Acknowledgement

This work was supported by the U.S. Department of Energy, Office of Science, Basic Energy Sciences, Materials Sciences and Engineering Division. Simulations were performed using PNNL Institutional Computing facility. PNNL is a multiprogram National Laboratory operated by Battelle for the U.S. Department of Energy under Contract DE-AC06-76RLO 1830.

5. Reference

References

- [1] G. Koch, J. Varney, N. Thompson, O. Moghissi, M. Gould, J. Payer, Nace international measures of prevention, application, and economics of corrosion technologies study, [Online; accessed 28-Feb-2018] (2016). <http://impact.nace.org/documents/Nace-International-Report.pdf>
- [2] H. W. Glea (Ed.), Vol. 2 of Proceedings of the 1st International Chromium Steel and Alloys Congress, SAIMM, 1992.
- [3] G. T. Van-Rooyen, The potential of chromium as an alloying element, in: H. W. Glea (Ed.), Chromium Steel and Alloys, Vol. 2 of Proceedings of the 1st International Chromium Steel and Alloys Congress, SAIMM, Cape Town, South Africa, 1992, pp. 43–47.
- [4] S. D. Cramer, J. B. S. Covino (Eds.), Corrosion: Materials, Vol. 13B, and Corrosion: Environment and Industries, Vol. 13C of ASM Handbook; ASM International: Materials Park, OH, USA, 2005.
- [5] G. S. Was, J. T. Busby, Role of irradiated microstructure and microchemistry in irradiation-assisted stress corrosion cracking, *Philos. Mag.* 85 (4-7) (2005) 443–465. doi:10.1080/02678370412331320224.
- [6] S. J. Zinkle, J. T. Busby, Structural materials for fission and fusion energy, *Mater. Today* 12 (11) (2009) 12 – 19. doi:10.1016/S1369-7021(09)70294-9.
- [7] D. Schreiber, M. Olsza, D. Saxey, K. Kruska, K. Moore, S. Lozano-Perez, S. Bruemmer, Examinations of oxidation and sulfidation of grain boundaries in alloy 600 exposed to simulated pressurized water reactor primary water, *Microscopy and Microanalysis* 19 (2013) 676–687. doi:10.1017/S1431927613000421.
- [8] D. Schreiber, M. Olsza, S. Bruemmer, Grain boundary depletion and migration during selective oxidation of cr in a ni-5cr binary alloy exposed to high-temperature hydrogenated water, *Scripta Materialia* 89 (2014) 41 – 44. doi:10.1016/j.scriptamat.2014.06.022.
- [9] P. Kofstad, K. Lillerud, Chromium transport through Cr_2O_3 scales i. on lattice diffusion of chromium, *Oxidation of metals* 17 (3-4) (1982) 177–194.
- [10] A. Sabioni, B. Lesage, A. Huntz, J. Pivin, C. Monty, Self-diffusion in Cr_2O_3 I. Chromium diffusion in single crystals, *Philosophical Magazine A* 66 (3) (1992) 333–350.
- [11] A. Sabioni, A. Huntz, F. Millot, C. Monty, Self-diffusion in Cr_2O_3 II. Oxygen diffusion in single crystals, *Philosophical Magazine A* 66 (3) (1992) 351–360.
- [12] A. Sabioni, A. Huntz, F. Millot, C. Monty, Self-diffusion in Cr_2O_3 III. Chromium and oxygen grain-boundary diffusion in polycrystals, *Philosophical Magazine A* 66 (3) (1992) 361–374.
- [13] K. Hoshino, N. Peterson, Cation self-diffusion in Cr_2O_3 , *Journal of the American Ceramic Society* 66 (11).
- [14] R. Latanision, R. Staehle, Stress corrosion cracking of iron–nickel–chromium alloys, Tech. rep., Ohio State Univ. Research Foundation, Columbus (1967).
- [15] E. Schmucker, C. Petitjean, L. Martinelli, P.-J. Panteix, S. B. Lagha, M. Vilasi, Oxidation of ni-cr alloy at intermediate oxygen pressures. i. diffusion mechanisms through the oxide layer, *Corrosion Science* 111 (2016) 474–485. doi:10.1016/j.corsci.2016.05.025.
- [16] P. Cao, D. Wells, M. P. Short, Anisotropic ion diffusion in $\alpha\text{-Cr}_2\text{O}_3$: an atomistic simulation study, *Phys. Chem. Chem. Phys.* 19 (2017) 13658.
- [17] F. Lebreau, M. M. Islam, B. Diawara, P. Marcus, Structural, magnetic, electronic, defect, and diffusion properties of Cr_2O_3 : A dft+u study, *J. Phys. Chem. C* 118 (31) (2014) 18133–18145. doi:10.1021/jp5039943.
- [18] B. Medasani, M. L. Sushko, K. M. Rosso, D. K. Schreiber, S. M. Bruemmer, Vacancies and vacancy-mediated self diffusion in cr_2o_3 : A first-principles study, *J. Phys. Chem. C* 121 (3) (2017) 1817–1831. doi:10.1021/acs.jpcc.7b00071.

- [19] C. Gray, Y. Lei, G. Wang, Charged vacancy diffusion in chromium oxide crystal: Dft and dft+u predictions, *J. Appl. Phys.* 120 (21) (2016) 215101. doi:10.1063/1.4970882.
- [20] J. Vaari, Molecular dynamics simulations of vacancy diffusion in chromium(iii) oxide, hematite, magnetite and chromite, *Solid State Ion.* 270 (2015) 10 – 17. doi:10.1016/j.ssi.2014.11.027.
- [21] L. Latu-Romain, Y. Parsa, S. Mathieu, M. Vilasi, A. Galerie, Y. Wouters, Towards the growth of stoichiometric chromia on pure chromium by the control of temperature and oxygen partial pressure, *Corrosion Science* 126 (2017) 238 – 246. doi:10.1016/j.corsci.2017.07.005.
- [22] P. Hohenberg, W. Kohn, Inhomogeneous electron gas, *Phys. Rev.* 136 (1964) B864–B871. doi:10.1103/PhysRev.136.B864.
- [23] W. Kohn, L. J. Sham, Self-consistent equations including exchange and correlation effects, *Phys. Rev.* 140 (1965) A1133–A1138. doi:10.1103/PhysRev.140.A1133.
- [24] J. P. Perdew, S. Kurth, in: C. Fiolhais, F. Nogueira, M. Marques (Eds.), *A Primer in Density Functional Theory*, Springer, Berlin, 1990.
- [25] C. Freysoldt, B. Grabowski, T. Hickel, J. Neugebauer, G. Kresse, A. Janotti, C. G. Van de Walle, First-principles calculations for point defects in solids, *Rev. Mod. Phys.* 86 (2014) 253–305. doi:10.1103/RevModPhys.86.253.
- [26] D. Broberg, B. Medasani, N. E. Zimmermann, G. Yu, A. Canning, M. Haranczyk, M. Asta, G. Hautier, Pycdt: A python toolkit for modeling point defects in semiconductors and insulators, *Computer Physics Communications* 226 (2018) 165 – 179. doi:10.1016/j.cpc.2018.01.004.
- [27] S. P. Ong, W. D. Richards, A. Jain, G. Hautier, M. Kocher, S. Cholia, D. Gunter, V. L. Chevrier, K. A. Persson, G. Ceder, Python materials genomics (pymatgen) a robust, open-source python library for materials analysis, *Comput. Mater. Sci.* 68 (2013) 314.
- [28] N. E. R. Zimmermann, M. K. Horton, A. Jain, M. Haranczyk, Assessing local structure motifs using order parameters for motif recognition, interstitial identification, and diffusion path characterization, *Frontiers in Materials* 4 (2017) 34. doi:10.3389/fmats.2017.00034.
- [29] G. Kresse, J. Hafner, *Ab initio* molecular dynamics for liquid metals, *Phys. Rev. B* 47 (1993) 558–561. doi:10.1103/PhysRevB.47.558.
- [30] G. Kresse, J. Hafner, *Ab initio* molecular-dynamics simulation of the liquid-metal*amorphous-semiconductor transition in germanium, *Phys. Rev. B* 49 (1994) 14251–14269. doi:10.1103/PhysRevB.49.14251.
- [31] G. Kresse, J. Furthmüller, Efficient iterative schemes for *ab initio* total-energy calculations using a plane-wave basis set, *Phys. Rev. B* 54 (1996) 11169–11186. doi:10.1103/PhysRevB.54.11169.
- [32] A. I. Liechtenstein, V. I. Anisimov, J. Zaanen, Density-functional theory and strong interactions: Orbital ordering in mott-hubbard insulators, *Phys. Rev. B* 52 (1995) R5467–R5470. doi:10.1103/PhysRevB.52.R5467.
- [33] A. Rohrbach, J. Hafner, G. Kresse, *ab initio* study of the (0001) surfaces of hematite and chromia: Influence of strong electronic correlations, *Phys. Rev. B* 70 (2004) 125426. doi:10.1103/PhysRevB.70.125426.
- [34] S. B. Zhang, J. E. Northrup, Chemical potential dependence of defect formation energies in GaAs: Application to ga self-diffusion, *Phys. Rev. Lett.* 67 (1991) 2339–2342.
- [35] G. Henkelman, B. P. Uberuaga, H. Jónsson, A climbing image nudged elastic band method for finding saddle points and minimum energy paths, *J. Chem. Phys.* 113 (2000) 9901–9904.
- [36] A. Togo, I. Tanaka, First principles phonon calculations in materials science, *Scr. Mater.* 108 (2015) 1–5.
- [37] K. Momma, F. Izumi, *VESTA3* for three-dimensional visualization of crystal, volumetric and morphology data, *J. Appl. Crystallogr.* 44 (2011) 1272–1276.
- [38] B. Huang, R. Gillen, J. Robertson, Study of ceo2 and its native defects by density functional theory with repulsive potential, *The Journal of Physical Chemistry C* 118 (42) (2014) 24248–24256. doi:10.1021/jp506625h.
- [39] A. B. Kehoe, E. Arca, D. O. Scanlon, I. V. Shvets, G. W. Watson, Assessing the potential of mg-doped cr₂o₃ as a novel p-type transparent conducting oxide, *Journal of Physics: Condensed Matter* 28 (12) (2016) 125501.
- [40] J. J. Carey, M. Legesse, M. Nolan, Low valence cation doping of bulk cr₂o₃: Charge compensation and oxygen vacancy formation, *The Journal of Physical Chemistry C* 120 (34) (2016) 19160–19174. doi:10.1021/acs.jpcc.6b05575.
- [41] S. Lany, Semiconducting transition metal oxides, *Journal of Physics: Condensed Matter* 27 (28) (2015) 283203.
- [42] C. Freysoldt, J. Neugebauer, C. G. Van de Walle, Fully ab initio finite-size corrections for charged-defect supercell calculations, *Phys. Rev. Lett.* 102 (2009) 016402. doi:10.1103/PhysRevLett.102.016402.
- [43] Y. Kumagai, F. Oba, Electrostatics-based finite-size corrections for first-principles point defect calculations, *Phys. Rev. B* 89 (2014) 195205. doi:10.1103/PhysRevB.89.195205.
- [44] A. Janotti, C. G. Van de Walle, Native point defects in zno, *Phys. Rev. B* 76 (2007) 165202.
- [45] Y. Lei, G. Wang, Linking diffusion kinetics to defect electronic structure in metal oxides: Charge-dependent vacancy diffusion in alumina, *Scripta Materialia* 101 (2015) 20 – 23. doi:10.1016/j.scriptamat.2015.01.008.